Remote Sensing of Environment 167 (2015) 20–30

Contents lists available at ScienceDirect

Remote Sensing of Environment

journal homepage: www.elsevier.com/locate/rse

Estimation of high-resolution land surface net shortwave radiation from AVIRIS data: Algorithm development and preliminary results

Tao He [a,*], Shunlin Liang [a,c], Dongdong Wang [a], Qinqing Shi [a], Michael L. Goulden [b]

[a] Department of Geographical Sciences, University of Maryland, College Park, MD 20742, USA
[b] Department of Earth System Science, University of California, Irvine, CA 92697, USA
[c] State Key Laboratory of Remote Sensing Science, School of Geography, Beijing Normal University, Beijing 100875, China

ARTICLE INFO

Article history:
Received 24 May 2014
Received in revised form 4 December 2014
Accepted 23 March 2015
Available online 16 April 2015

Keywords:
Hyperspectral
AVIRIS
HyspIRI
Surface albedo
Downward shortwave radiation
Net shortwave radiation
Direct estimation

ABSTRACT

Hyperspectral remote sensing provides unique and abundant spectral information for quantification of the land surface shortwave radiation budget, which can be used to calibrate climate models and to estimate surface energy budget for monitoring agriculture and urban environment. However, only single broadband or multispectral data have been used in previous studies. In the present study, two methods are proposed to estimate the instantaneous land surface net shortwave radiation (NSR) with high spatial resolutions using hyperspectral remote sensing observations from the Airborne Visible Infrared Imaging Spectrometer (AVIRIS) data. Method A calculates the NSR based on separate estimation of downward radiation and surface broadband albedo, which requires ancillary information for aerosol optical depth; and Method B directly estimates the NSR from the observed radiance. Results based on radiative transfer simulations showed that the use of hyperspectral data can significantly improve NSR estimation compared with the multispectral data method. Atmospheric water vapor correction was applied to adjust the surface radiation estimation. Validation of AVIRIS NSR estimates against ground measurements from two flux networks for the period of 2006–2014 showed that the two methods were similar and had consistent accuracy in the all-sky instantaneous NSR estimation with root-mean-square-errors (RMSEs) of approximately 28–56 W/m^2. The pixel-based water vapor content estimation from AVIRIS data provided slightly different results than those obtained using coarse resolution remote sensing data. A simplified topographic correction algorithm was found to be able to improve the results generated from Method A; however, the degree of improvement provided by Method B was unclear, possibly because of the lack of consideration of horizontal atmospheric scattering effects from adjacent pixels. In general, hyperspectral remote sensing data have been shown to improve the NSR estimation accuracies compared with results obtained in previous studies. Additional efforts are needed to refine the NSR estimation for application to future satellite hyperspectral data.

1. Introduction

Surface net shortwave radiation (NSR) is an important variable in the land surface energy balance, which regulates the Earth's climate through variations in surface properties, such as albedo, and atmospheric properties, such as aerosols, water vapor, and clouds (Liang, Wang, Zhang, & Wild, 2010; Wild et al., 2013).

Through decades of refinement in land surface radiation budget modeling, understanding of the Earth's radiation budget has greatly improved (e.g., Kiehl & Trenberth, 1997; Liang, Zhang, He, Cheng, & Wang, 2013; Pinker, Frouin, & Li, 1995; Stephens et al., 2012; Trenberth, Fasullo, & Kiehl, 2009; Wild, 2005, 2008; Wild et al., 2013). However, a comparison among the most recent climate models showed that there is still a gap of more than 10 W/m^2 in the global annual mean surface NSR from the climate model simulations (Wild et al., 2013).

Satellite observations provide unique data that are used to monitor climate change and its interaction with the land surface radiation budget on a global basis, which has been used as a key source of observational evidence in accuracy assessment for model simulations. During the past several decades, many NSR data sets have been developed from satellite observations. International Satellite Cloud Climatology Project (ISCCP) data at a spatial resolution of 2.5° were derived from the revised Goddard Institute for Space Studies (GISS) General Circulation Model (GCM) radiative transfer model with improved observations of the physical properties of the surface, atmosphere, and clouds from the ISCCP data sets (Zhang, Rossow, Lacis, Oinas, & Mishchenko, 2004). The Clouds and Earth's Radiant Energy Systems (CERES) Energy Balanced and Filled (EBAF) data are available at a spatial resolution of 1° (Loeb et al., 2012, 2009). The Global Energy and Water-cycle Experiment (GEWEX) Surface Radiation Budget (SRB) data were generated using a radiative transfer algorithm

* Corresponding author at: Department of Geographical Sciences, University of Maryland, 2181 LeFrak Hall, College Park, MD 20742, USA.Tel.: + 1 301 405 4538; fax: + 1 301 314 9299.
E-mail address: the@umd.edu (T. He).

http://dx.doi.org/10.1016/j.rse.2015.03.021
0034-4257/

that uses ISCCP cloud parameters and meteorological inputs from reanalysis data (Pinker & Laszlo, 1992; Stackhouse et al., 2011). However, in addition to the limitation posted by their coarse spatial resolutions, the uncertainties in the existing data remain relatively large for a refined understanding of the Earth's surface radiation budget (e.g., Gui, Liang, Wang, Li, & Zhang, 2010; He, Liang, & Song, 2014; Qin et al., 2011; Shi & Liang, 2013). A generally accepted global data set on the land surface shortwave radiation budget from observations, which could be used to calibrate the bias found in current climate model simulations, is still not available (Wild et al., 2013).

NSR varies both spatially and temporally. In addition to calibrating the coarse resolution climate models, there has been an increasing need for high-resolution land surface shortwave radiation data in surface energy balance modeling and in agricultural, ecological, and urban environmental studies (e.g., Kuusinen, Tomppo, Shuai, & Berninger, 2014; Roberts, Quattrochi, Hulley, Hook, & Green, 2012; Seyednasrollah & Kumar, 2013; Tasumi, Allen, & Trezza, 2008). To satisfy the needs for such research applications, NSR estimation at finer resolutions (<1 km) is required. In addition, high-resolution NSR estimation is critical to bridge the gap between coarse resolution products and ground measurements and for validating and calibrating coarse resolution data (Wang, Liang, & He, 2014). Algorithms have been derived using satellite observations with finer resolutions than those used in climate models, from sensors such as the moderate resolution imaging spectroradiometer (MODIS) (Bisht & Bras, 2010, 2011; Bisht, Venturini, Islam, & Jiang, 2005; Huang, Liu, & Liang, 2012; Hwang, Choi, Lee, & Seo, 2013; Kim & Liang, 2010) and Landsat (Dubayah, 1992; Wang et al., 2014; Wang, White, & Robinson, 2000). However, the uncertainties in instantaneous NSR estimation from those algorithms and data remain relatively large with root-mean-square-errors (RMSEs) ranging from approximately 50 W/m^2 to more than 100 W/m^2, which is far beyond the uncertainty threshold specified by the World Meteorological Organization (WMO) observation requirements (http://www.wmo-sat.info/db/variables/view/50, updated on June 23, 2011).

Estimation of the NSR at a finer resolution is helpful for verifying the existing products from satellite observations, reanalysis data, and model simulations, which is otherwise difficult using ground measurements because of the scale differences. NSR has generally been estimated through the calculation of downward shortwave radiation (DSR) and surface albedo (Wang et al., 2000). However, high-resolution products of both data sets are scarcely available. For cloudy-sky conditions, surface albedo cannot be estimated from instantaneous satellite observations; this type of approach can work only for clear-sky conditions. Algorithms that directly link sensor-observed radiance and NSR have been recently developed to bridge the gap for cloudy-sky NSR estimation (Kim & Liang, 2010; Wang et al., 2014).

Hyperspectral data present unique advantages in the detection of ecosystem response to climate variability through their abundant spectral information (Garcia & Ustin, 2001; Schaepman et al., 2009). In a previous study, algorithms for estimating surface broadband albedo directly from observed hyperspectral radiance or reflectance were developed and validated against ground measurements and Landsat albedo estimates showing RMSEs ranging between 0.027 and 0.032 (He, Liang, Wang, Shi, & Tao, 2014). However, to the best of our knowledge, the estimation of NSR has seldom been attempted using hyperspectral remote sensing data.

The main objective of this study is to demonstrate the potential of using hyperspectral data in the estimation of instantaneous NSR. It includes two specific objectives: prototyping the algorithms for estimating NSR from hyperspectral remote sensing data using the Airborne Visible/Infrared Imaging Spectrometer (AVIRIS) as proxy data and validating the preliminary results on NSR estimation from the proxy data against ground measurements. In this study, two types of approaches based on existing algorithms are implemented to estimate the NSR.

Method A is based on separate estimations of DSR and surface albedo for calculating the NSR. Surface albedo estimation is adopted from the direct estimation approach (He, Liang, Wang, Shi, et al., 2014). DSR is calculated by estimating surface reflectance and atmospheric transmittance using ancillary information on aerosol loadings.

Method B follows a similar empirical procedure for direct estimation of surface albedo by using simulations of observed radiance and surface flux from radiative transfer codes to train the regression models in order to estimate the NSR directly from the observed radiance.

The overall methodology for the two NSR estimation algorithms is described in Section 2, followed by the introduction of AVIRIS data and ground measurements. Section 3 presents the analysis and discussion on the results of NSR estimations from the two approaches.

2. Data and methodology

2.1. Methodology

In this study, two methods are proposed to estimate surface NSR from hyperspectral data (Fig. 1). The first method (Method A) calculates the NSR as the product of DSR and surface albedo (shown in the left section of Fig. 1). Surface albedo is pre-calculated from sensor-observed reflectance using a direct estimation approach. DSR is estimated from observed radiance after applying the atmospheric, elevation, and topographic correction. The second method (Method B) estimates the NSR directly from observed radiance based on the empirical relationship established from radiative transfer simulations, which is shown in the right section of Fig. 1. Water vapor, elevation, and topography effects are also considered in Method B.

2.1.1. Estimation of NSR based on albedo and DSR (Method A)

Method A is used to estimate NSR based on separate estimations of surface broadband albedo and DSR.

2.1.1.1. Albedo. To overcome the limitation of having reduced angular information from hyperspectral data, a direct estimation method was proposed in an earlier study (He, Liang, Wang, Shi, et al., 2014) for estimating surface broadband albedo directly from observed hyperspectral reflectance on an angular-bin basis. The results of that study show that the abundant spectral information can compensate for the lack of angular information in broadband albedo estimation.

2.1.1.2. DSR. DSR is a function of solar irradiance, solar zenith angle, and atmospheric properties, and is also to a lesser extent a function of surface reflectance, which can be estimated using a method proposed by Liang et al. (2006). In their method, the downward radiation was estimated using a time series of sensor observations based on simultaneous retrieval of surface and atmospheric properties (Liang et al., 2006, 2007; Liu, Liang, He, Liu, & Zheng, 2008; Zheng, Liang, & Wang, 2008).

$$\rho_t = \rho_a(\theta_s, \theta_v, \varphi) + \frac{\rho_s}{1-\rho_s S} T(\theta_s) T(\theta_v) \tag{1}$$

$$F(\theta_s) = F_0(\theta_s) + \frac{\rho_s S}{1-\rho_s S} \mu_s E_0 T(\theta_s) \tag{2}$$

$$DSR = \int_{300}^{4000} F_\lambda(\theta_s) d\lambda \tag{3}$$

where $\rho_a(\theta_s, \theta_v, \varphi)$ is the intrinsic reflectance of the atmosphere with solar zenith angle θ_s, view zenith angle θ_v, and relative azimuth angle φ, ρ_s is the surface reflectance, S is the spherical albedo of the atmosphere, $T(\theta_s)$ is the total transmittance (direct plus diffuse) from the top-of-atmosphere to the ground in the solar direction, $T(\theta_v)$ is the transmittance from the ground to the sensor in the viewing direction

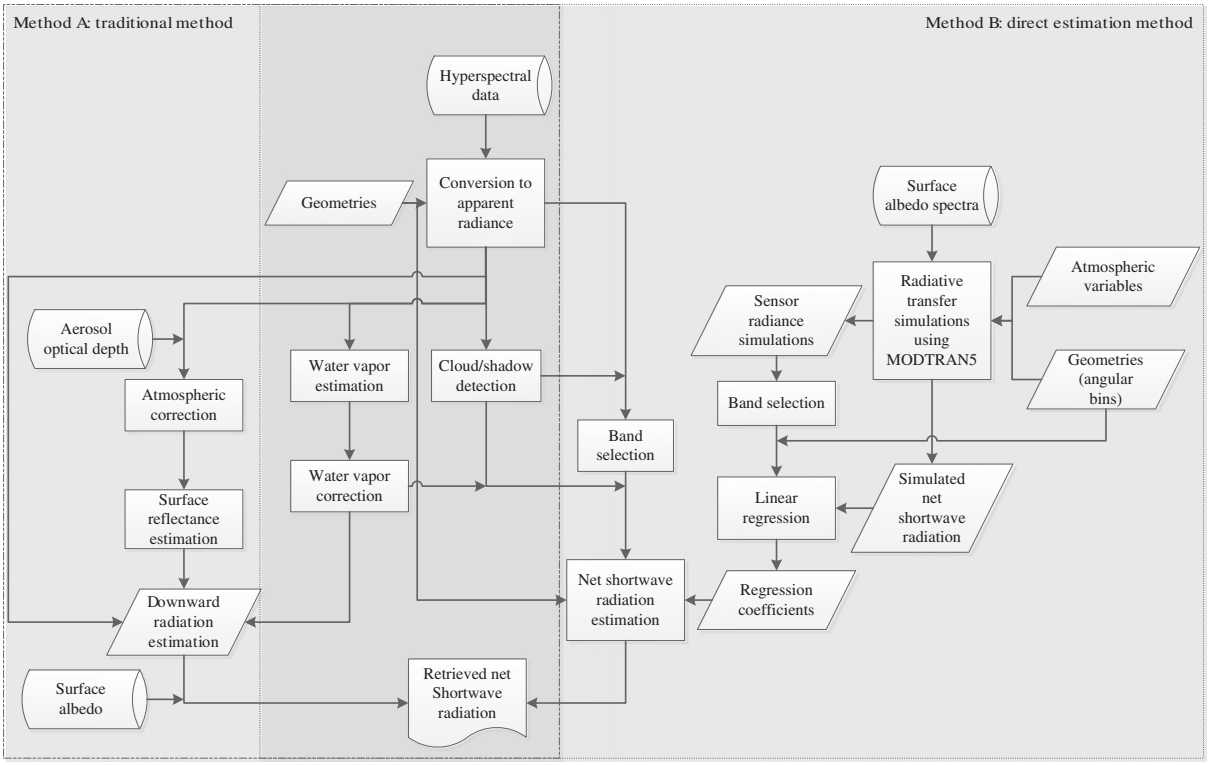

Fig. 1. Flowchart of two methods used to estimate surface net shortwave radiation (NSR) from hyperspectral data. Cylindrical boxes represent the input data; rectangular boxes stand for data process; other parallelograms stand for input parameters; the one irregular shape at the bottom is the final output. The flowchart for estimating surface albedo can be found in Fig. 1 of He, Liang, Wang, Shi, et al. (2014).

of the satellite, $F(\theta_s)$ is the surface downward flux at the specified solar zenith angle, $F_0(\theta_s)$ is the downward flux without any contribution from the surface, μ_s is the cosine of θ_s, and E_0 is the extraterrestrial solar irradiance. DSR is the integrated downward flux in the solar spectral domain 300–4000 nm. Owing to the lack of time series observations within a short period, the aerosol optical depth obtained from MODIS product was applied for atmospheric correction to estimate the surface reflectance ρ_s in this study.

Hyperspectral remote sensing data provide spectral samplings of the radiance usually in a narrower spectral range than the solar spectral domain. Thus, the estimation of spectral downward radiation needs to be integrated and converted to the total shortwave radiation by using Eq. (4) instead of Eq. (3). Because the water vapor absorption bands are not directly included in the estimation of DSR radiation in this study, a correction method is used to account for the water vapor effects on DSR estimation:

$$DSR = \int_{300}^{4000} F_\lambda d\lambda = c(\omega) \cdot \left(a \cdot \sum_{i \in B} F_i + b \right) \quad (4)$$

where F_λ and F_i represent the downward radiation of the wavelength λ, and the spectral band i of remote sensing data, respectively; B is the subset of spectral bands excluding the water vapor absorption and low single-to-noise-ratio (SNR) bands; a and b are the coefficients for the conversion of cumulated downward radiation from spectral bands to the DSR; and $c(\omega)$ is the water vapor correction factor determined by the amount of water vapor content ω (g/cm^2) retrieval, which is described in Section 2.2.

DSR estimation for clear-sky pixels is straightforward, following the procedure described in Eqs. (1), (2), and (4). Information on aerosol optical depth can be obtained from the MODIS level 2 product (Levy et al., 2010). Unlike that for the clear-sky pixels, the case for cloudy/shadow pixels is complicated for high-resolution data, particularly if the relative azimuth angle is beyond 90° and solar zenith angle is relatively large. In such cases, the major part of the shadow cast by a cloud can be easily identified from the image. Thus, the shadow pixels are the actual pixels without direct solar radiation; however, when the pixels are identified as clouds, it is largely unknown whether the land surface corresponding to those pixels received direct sunlight. For the sake of simplicity, the cloud and shadow pixels are treated in the same manner in the DSR estimation using diffuse radiation simulated under the actual illumination geometries and aerosol loadings with water vapor correction. The NSR can then be calculated based on the estimation of surface albedo and DSR. Information on the radiative transfer simulation can be found in Section 2.4.

2.1.2. Direct estimation of NSR (Method B)

Based on a principle similar to that used for broadband albedo direct estimation, NSR can be directly estimated from the observed radiance using the following relationship:

$$NSR = \sum_{i \in B} a_i L_i + a_0 \quad (5)$$

where L_i represents the observed radiance for band i, B is the subset of the spectral bands, and a_0 and a_i are the regression coefficients in the linear relationship.

To generate the regression coefficients in Eq. (5), the observed at-sensor radiances for the spectral bands and surface broadband flux are first simulated by using radiative transfer models under various illumination and atmospheric conditions, and over different surface types. Details on the radiative transfer simulations can be found in Section 2.4. The simulated NSR, calculated from the surface broadband flux, is regressed against the spectral radiance L_i on an angular-bin basis to generate the regression coefficients. To reduce the uncertainty of the linear regression, spectral bands with low SNR are not considered. In addition, water vapor variation can result in large differences in observed radiance for major water vapor absorption bands, which

leads to a high-order empirical relationship between NSR and observed radiance. Thus, major water vapor bands are not considered in the establishment of the linear relationship.

2.2. Water vapor estimation and correction

Water vapor has strong absorptions in several wavelength ranges in the shortwave spectrum, particularly in the shortwave infrared range including 0.94, 1.14, 1.38, and 1.88 μm. Variation in the atmospheric water vapor could cause changes in DSR. An uncertainty of 2% in the water vapor estimation can lead to an error of approximately 1 W/m^2 in the DSR estimation (Revercomb et al., 2003). Thus, water vapor effects need to be corrected for the surface radiation estimation.

Various algorithms have been developed for estimating precipitable water from hyperspectral remote sensing sensors (Gao, Montes, Davis, & Goetz, 2009; Liang & Fang, 2004). Because water vapor varies spatially and temporally, a pixel-based water vapor algorithm without the support of surface reflectance measurement is needed for estimation of the surface radiation budget. In this study, the continuum interpolated band ratio (CIBR) algorithm (Bruegge et al., 1992; Kaufman & Gao, 1992) is adopted to estimate water vapor content from the AVIRIS data. Liang and Fang (2004) applied the CIBR method on AVIRIS data using a combination of three bands including 885, 943, and 1039 nm:

$$CIBR = \frac{L_{943nm}}{0.628L_{885nm} + 0.372L_{1039nm}} \tag{6}$$

$$\log(CIBR) = -0.663545\omega^{0.6358} \tag{7}$$

Here, L_λ is the observed radiance of band λ, and ω is the column water vapor content (g/cm^2). The coefficients are determined based on simulation data sets that considered variations in atmospheric water vapor, aerosols, and surface reflectance spectra (Liang & Fang, 2004).

2.3. Correction for elevation and topographic effects

Surface elevation that controls the atmospheric mass can affect the Rayleigh scattering and can thus impact surface radiation budget. In the radiative transfer simulations, only the flux data at sea-level elevation are used for the surface radiation estimation. However, flux data for different surface elevations can be simulated by using the radiative transfer codes. The method proposed in Kim and Liang (2010) is used for the elevation correction based on radiative transfer simulations.

Topographic effects can play an important role in determining the DSR and NSR, particularly in mountainous regions. Due to the lack of both precise digital elevation models available at AVIRIS spatial resolution and the hyperspectral surface anisotropy information, several recently developed algorithms for topographic correction (e.g., Li et al., 2012; Wen, Zhao, Liu, Tang, & Dou, 2014) cannot be directly applied to AVIRIS data. To mitigate the topographic effects, a simple correction method for the observed radiance/reflectance can be applied to correct the viewing zenith angle θ_v' on the basis of topographic information:

$$\cos(\theta_v') = \cos(\theta_v)\cos(s) + \sin(\theta_v)\sin(s)\tan(|\gamma - \varphi_v|) \tag{8}$$

where θ_v is the nominal view zenith angle, s is the slope, γ is the aspect, and φ_v is the view azimuth angle, which are provided along with the AVIRIS data as well as the corrected solar zenith angle θ_s.

The corrected geometries are then incorporated into the estimation method mentioned in Section 2.1.

2.4. Model simulations

The fifth version of the MODerate resolution atmospheric TRANsmission (MODTRAN5) software package (Berk et al., 2006) is used in this study to simulate the observed at-sensor radiance and fluxes for each of the spectral bands under various atmospheric and illumination conditions (Table 1 in He, Liang, Wang, Shi, et al., 2014). Two hundred forty-five surface albedo spectra including those for vegetation, soil, rock, water, snow, and ice from surface spectral libraries (Baldridge, Hook, Grove, & Rivera, 2009; Clark et al., 2007) are used in the simulations. Settings for the atmospheric profile, default precipitable water, and aerosol type are adopted from our previous study (He, Liang, Wang, Shi, et al., 2014). Because the cloud type does not have a significant impact on the NSR estimation (Kim & Liang, 2010), stratus/stratocumulus clouds are used in this study for cloudy-sky simulations. To estimate the radiation components, a separate set of simulations for the total shortwave range (300–4000 nm) is conducted using the same settings as those for atmospheric and illumination conditions. Given that the pyranometers used for in-situ measurements of flux usually cover the spectral range of 300–2800 nm and that the downward shortwave radiation beyond 2800 nm is relatively small, the difference between the radiation estimates in this study and in-situ measurements are assumed to be negligible. The output data sets from the MODTRAN simulations include the observed radiance (also known as apparent radiance), downward and upward radiation for the spectral bands and the total shortwave both at sensor altitude and surface, and the atmospheric variables used in Eqs. (1) and (2). The apparent spectral reflectance, surface shortwave albedo, and surface NSR can then be calculated or integrated based on these output data.

2.5. AVIRIS data

AVIRIS is an air-borne sensor operated by the United States National Aeronautics and Space Administration (NASA) Jet Propulsion Laboratory (JPL) and usually flies on ER-2 and Twin Otter aircrafts mainly over the United States. The AVIRIS sensor consists of 224 spectral bands in the range of ~360 nm to ~2500 nm with an average bandwidth of ~10 nm. The spatial resolution of AVIRIS data varies from ~3 m to ~17 m depending on the flight altitude. The AVIRIS data from 2006 to 2014 used in this study have been orthorectified and radiometrically calibrated; and are publicly available through the JPL website (http://aviris.jpl.nasa.gov/data/get_aviris_data.html).

Active since early 2013, the Hyperspectral Infrared Imager (HyspIRI) flight campaign carries recently calibrated AVIRIS sensor onboard to provide observations over several key study areas in California, USA, for various seasons. Because the HyspIRI campaign tended to obtain flight data under cloud-free conditions, the majority of the flight data were either free of clouds or contained a small amount of scattered clouds. To mitigate the topographic effects in the mountainous regions in the HyspIRI flight areas, the topographic correction method described in Section 2.3 for the observed radiance/reflectance is tested on the basis of slope and aspect information provided along with the AVIRIS flight data. Detection of clouds and shadows is conducted using a Gaussian distribution matching method based on the histogram of a water vapor band at 1.38 μm (Gao, Goetz, & Wiscombe, 1993; Gao & Kaufman, 2003; He, Liang, Wang, Shi, et al., 2014). Visual interpretation of the AVIRIS images is incorporated into this preprocessing to correct spurious results and to ensure at least 95% accuracy on the classification of clouds and shadows. Possible improvement of cloud and shadow detection, however, is beyond the scope of the present study.

2.6. Ground measurements

Ground measurements of downward and upward shortwave radiation from AmeriFlux sites over North America are publicly available. At the time of this study, the 2014 data from AmeriFlux were not yet available and; thus, only the flight data before 2014 were used for validation at the AmeriFlux sites. In addition, ground measurements are obtained at several sites in the Sierra Nevada and Southern regions of California, USA, during 2006–2014; these sites are referred to hereafter as the University of California Irvine (UCI) network (Goulden et al., 2012).

These measurements are made using up and down looking Kipp & Zonen CM3 pyranometers with means recorded every 30 min. Most pyranometers have an uncertainty of approximately ±5% in flux measurements and sometimes worse as a result of factors such as possible instrument drift and leveling. Surface albedo can be calculated by dividing the upward to the downward radiation. Net radiation is the difference between downward and upward radiation. Average values of the surface radiation components are calculated using observations within ±1 h of the flight overpass time for validation purposes.

All of the available AVIRIS data acquired during overpasses above the ground stations for the period of 2006–2014 were cross-checked against available ground measurements. Matches for the AmeriFlux sites were tabulated in Table 2 in He, Liang, Wang, Shi, et al. (2014). Table 1 lists the information for the AVIRIS flights over the Sierras and Southern California. It is worthy to note that all the AVIRIS data over the UCI sites are clear-sky scenes with nominal cloud coverages of less than 20%. This number is used as a threshold to separate clear-sky scenes and cloudy scenes in this study.

Table 1
List of Airborne Visible Infrared Imaging Spectrometer (AVIRIS) flight with overpasses above sites from the University of California Irvine (UCI) network.

Site	Lat/lon (°N, °E)	Flight no.	Year	DOY	UTC
LR_Grass	33.7365, −117.6946	f060510t01p00r04	2006	130	21:20
		f140414t01p00r11	2014	104	20:36
		f140419t01p00r06	2014	109	22:15
		f140613t01p00r10	2014	164	20:34
		f140613t01p00r12	2014	164	21:52
LR_Sage	33.7343, −117.6959	f060510t01p00r03	2006	130	21:09
		f060510t01p00r04	2006	130	21:20
		f130412t01p00r11	2013	102	21:25
		f130419t01p00r12	2013	109	21:25
		f130924t01p00r11	2013	267	20:33
		f140414t01p00r11	2014	104	20:36
		f140419t01p00r06	2014	109	22:15
		f140613t01p00r10	2014	164	20:34
		f140613t01p00r12	2014	164	21:52
Jreserve	33.8079, −116.7717	f140414t01p00r14	2014	104	22:31
DC_Pinyon	33.6049, −116.4547	f140613t01p00r06	2014	164	18:02
		f140613t01p00r09	2014	164	19:57
DC_Burn	33.6100, −116.4502	f060506t01p00r12	2006	126	18:56
		f130412t01p00r07	2013	102	18:52
		f130419t01p00r08	2013	109	18:52
		f130924t01p00r07	2013	267	18:03
		f140414t01p00r12	2014	104	21:14
		f140613t01p00r06	2014	164	18:02
SJER	37.1087, −119.7313	f130503t01p00r17	2013	123	20:44
		f130612t01p00r09	2013	163	18:00
		f140407t01p00r09	2014	97	19:11
		f140407t01p00r11	2014	97	19:48
		f140603t01p00r17	2014	154	20:25
Soaproot	37.0311, −119.2563	f130503t01p00r15	2013	123	20:06
		f130503t01p00r22	2013	123	22:18
		f130606t01p00r05	2013	157	18:25
		f130612t01p00r07	2013	163	17:26
		f130612t01p00r14	2013	163	19:25
		f130626t01p00r07	2013	177	18:20
		f140407t01p00r07	2014	97	18:34
		f140407t01p00r16	2014	97	21:08
		f140410t01p00r18	2014	100	21:31
		f140603t01p00r10	2014	154	18:11
		f140603t01p00r12	2014	154	18:48
		f140603t01p00r21	2014	154	21:41
P301	37.0673, −119.1948	f130612t01p00r14	2013	163	19:25
		f130626t01p00r09	2013	177	18:54
		f140407t01p00r16	2014	97	21:08
		f140410t01p00r18	2014	100	21:31
		f140603t01p00r10	2014	154	18:11
		f140603t01p00r12	2014	154	18:48

DOY: Day of year; UTC: Coordinated Universal Time.

3. Results and discussion

3.1. Water vapor estimation

To validate the water vapor estimation in this study, the precipitable water data derived from in-situ measurements available from the Global Positioning System (GPS) stations in the SuomiNet Network in the United States (Bevis et al., 1994; Braun & Van Hove, 2005) were used for comparison. The in-situ data are available at hourly intervals from late 2009 to the present and can be accessed online at http://www.suominet.ucar.edu/data.html. There were 113 corresponding AVIRIS flight overpasses at the GPS stations from 2009 to 2013. Estimation of total water vapor content from AVIRIS data aggregated to 5 km was validated against the GPS in-situ measurements with the closest acquisition time to the flights. Results shown in Fig. 2 suggest that the CIBR algorithm can achieve reasonable accuracy for water vapor content with a slight positive bias of 0.128 g/cm^2 and an RMSE of 0.385 g/cm^2.

Large water vapor contents were not identified through the comparison due to the limited number of flights over the GPS stations. To further verify the CIBR algorithm, the AVIRIS water vapor estimation obtained over 15 AmeriFlux sites from 2006 to 2012 were spatially aggregated and rescaled to match with the 1 km MODIS water vapor product (MOD05); the latter is believed to have an accuracy of 5–10% (Gao & Kaufman, 2003). From the comparison shown in Fig. 3, the AVIRIS estimation generally agrees quite well with the MODIS water vapor product with an R^2 of 0.882. An exception of a slight overestimation occurred in the AVIRIS results, however, when the MODIS data were 1–2 g/cm^2. Impacts of this difference on surface radiation estimation are discussed in the Section 3.2.

3.2. Estimation of NSR based on albedo and DSR (Method A)

3.2.1. Direct estimation of surface albedo

Surface shortwave albedo, defined as the ratio of the outgoing to the incoming solar radiation at the Earth's surface, is a very important biophysical variable in climate and ecological studies. Surface broadband albedo is the integrated value of the atmospherically corrected surface directional reflectances over the entire hemisphere for the total shortwave spectrum. It is difficult to obtain sufficient angular sampling over the same surface target from AVIRIS flights in order to implement the angular integration. To overcome this limitation, a number of algorithms have been developed to estimate the instantaneous surface broadband albedo with reduced angular samples based on empirical relationships (He, Liang, Wang, Shi, et al., 2014; He et al., 2012; Liang,

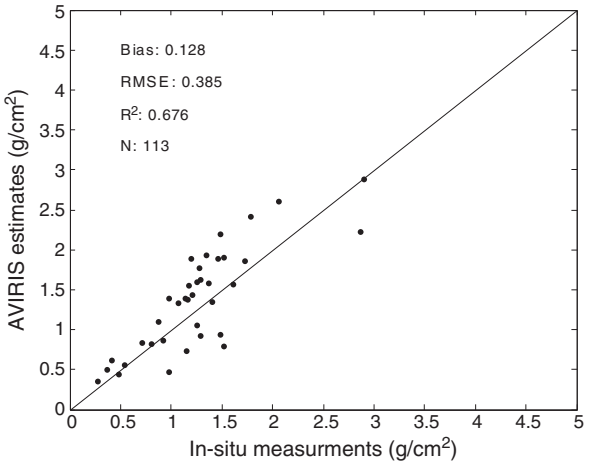

Fig. 2. Comparison of AVIRIS water vapor estimation and GPS in-situ measurements from SuomiNet Network. The ratio of bias to mean in-situ values is 10.25%. Statistics are significant at the 95% confidence level.

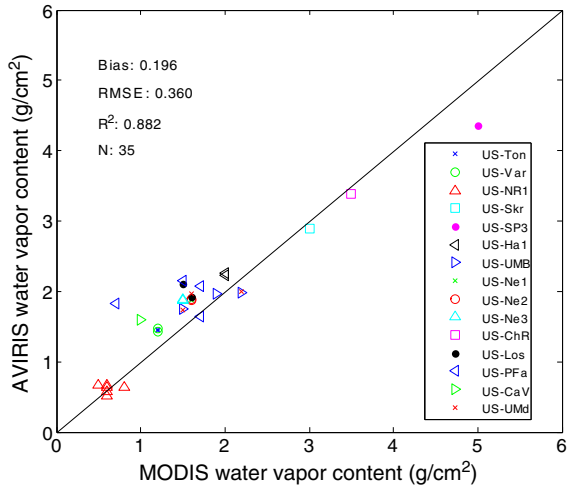

Fig. 3. Comparisons of spatially aggregated AVIRIS water vapor retrievals and MOD05 product at AmeriFlux sites. The ratio of bias to mean MODIS values is 12.44%. Statistics are significant at the 95% confidence level.

Stroeve, & Box, 2005; Wang, Liang, He, & Yu, 2013). In particular, it has been proven that the hyperspectral information from AVIRIS data can compensate for the lack of angular information and does not result in significant errors for surface broadband albedo estimation over snow-free surfaces (He, Liang, Wang, Shi, et al., 2014).

Given that AVIRIS has 224 bands and many bands are inter-correlated, simply applying direct estimation by using all the bands is not necessary and may even cause over-fitting problems. Therefore, water vapor absorption bands and low SNR bands were removed in the direct estimation of surface albedo and surface radiation. Two algorithms have been tested including a stepwise regression and a Principle Component Analysis (PCA)-based regression, which directly estimate surface broadband albedo from the observed radiance/reflectance. Comparisons showed that estimation results agreed well with validation data sets for both algorithms. In particular, the PCA-based regression algorithm was validated against ground measurements and Landsat albedo with respective RMSEs of 0.027 and 0.032.

For the albedo and NSR validation, the footprint of the pyranometers (upward flux) is critical in the comparison of remote sensing data and ground measurements in terms of surface heterogeneity due to scale differences (Roman et al., 2011, 2013, 2009). The actual footprint for each of the pyranometers was calculated based on its height and field-of-view (He, Liang, Wang, Shuai, & Yu, 2014; Shuai, Masek, Gao, & Schaaf, 2011) obtained from both networks.

The comparison shown in Fig. 4 indicates that the proposed surface albedo direct estimation algorithm works well for the sites from both networks with respective RMSEs of 0.032 and 0.022. Although some sites from UCI network are located in mountainous areas, the area immediately around the tower and the footprint of the radiation measurements (particularly the upward radiation) for most sites is fairly flat (<10°). The albedo estimation with topographic correction has similar accuracy with an RMSE of 0.020. This suggests that topographic correction is not the key issue in the albedo validation in this study. However, additional ground measurements over other mountainous regions would be highly useful in investigating the performance of topographic correction in albedo estimation.

3.2.2. DSR

As previously mentioned, the downward radiation was simulated for the total shortwave range and for the AVIRIS spectral bands, respectively, under different illumination and atmospheric conditions. The cumulated downward radiation $\sum_{i \in B} F_i$ from AVIRIS bands is lower than the simulated DSR from MODTRAN (Fig. 5) for several reasons. First,

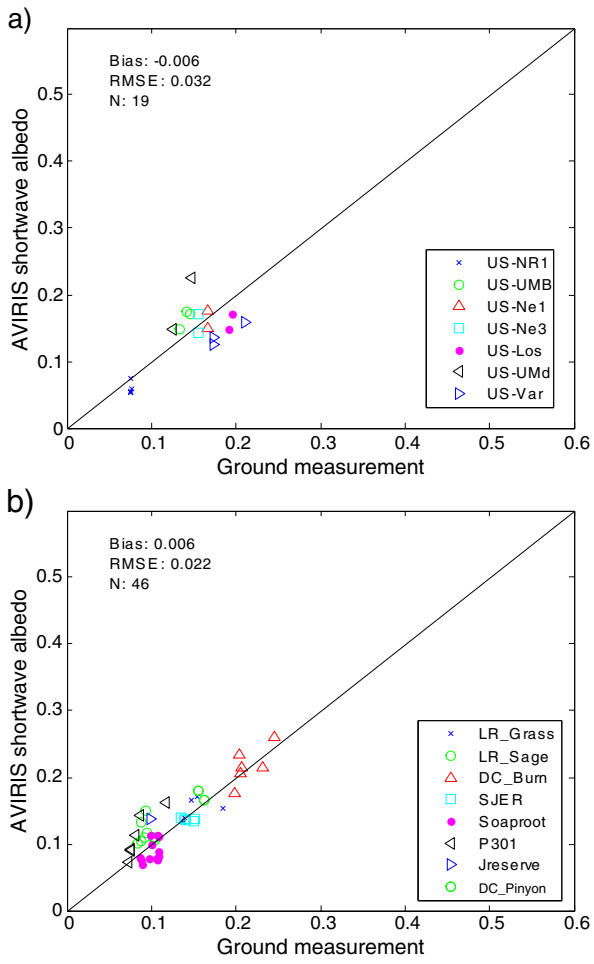

Fig. 4. Validation of surface shortwave albedos at sites from (a) AmeriFlux network and (b) UCI network.

the downward radiation in the wavelength range for water vapor absorption and low-SNR bands was not included. Second, even if all the AVIRIS bands were included, a gap would still exist between the AVIRIS spectral coverage and the total shortwave range. Third, overlap among AVIRIS bands makes it impossible to directly sum up the downward radiation from all of the bands to obtain the DSR. The comparison shown in Fig. 5 indicates that the conversion from narrowband to

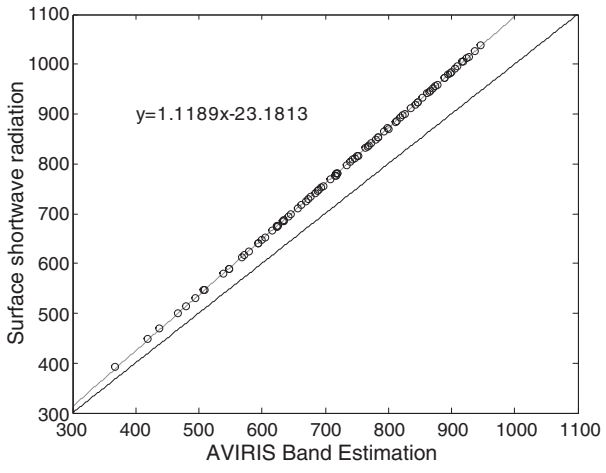

Fig. 5. Conversion of cumulated radiation from AVIRIS bands to shortwave radiation (W/m^2).

broadband radiation for Eq. (4) (a = 1.12, b = −23.18) is very stable under various illumination geometries and atmospheric conditions.

Water vapor can absorb a relatively significant amount of solar radiation, particularly in the infrared spectrum. The effects of water vapor absorption on the DSR were simulated by varying the water vapor content in the MODTRAN simulations, which can help understand the behavior of the correction factor $c(\omega)$ in Eq. (4). Fig. 6a suggests that $c(\omega)$ decreases as the water vapor content increases; $c(\omega)$ varies between 0.91 and 1.05 when the water vapor content ranges between 0.5 g/cm^2 and 7.0 g/cm^2. This variation can be explained by several facts. Water vapor absorbs solar shortwave radiation mainly in the near infrared spectrum, which contains downward shortwave radiation of approximately 53% of the total solar radiation (Papaioannou, Papanikolaou, & Retalis, 1993). Moreover, larger water vapor content can absorb more solar radiation. Compared with the default water vapor content set at 3.0 g/cm^2 in the MODTRAN simulations, the variation in water vapor content from 0.5 to 7.0 g/cm^2 can cause a difference of approximately −10% to +5% in the DSR estimation. The effects of aerosol loading and illumination geometries are relatively weak in the water vapor correction and contribute to a lower order of magnitude for the correction factor $c(\omega)$, as shown in Fig. 6b. This occurs likely because aerosol tends to have a much smaller scattering effect in the longer wavelengths than that in the visible spectral range. Thus, the interaction of water vapor and aerosol is relatively weak in major water vapor absorption bands in the near/shortwave infrared spectrum. As the water vapor content increases to ~7.0 g/cm^2, its absorption in the shorter wavelengths then interacts with aerosol scattering in the DSR, which is indicated in Fig. 6b with an increased standard deviation (SDEV) for large water vapor content values. This water vapor correction was also applied for NSR direct estimation (Method B).

Validation of the DSR and NSR estimation following Method A was made at both networks using a 5-km spatial window similar to the one used for the validation of water vapor. For AmeriFlux sites (Fig. 7), the overall accuracy for the all-sky DSR estimation is satisfactory with a bias and RMSE of −10.3 W/m^2 and 55.7 W/m^2, respectively. With a small amount of solar energy reflected back to the sky, the NSR was estimated with a bias of −3.8 W/m^2 and an RMSE of 29.6 W/m^2. The error found in both the DSR and NSR estimation is largely caused by an outlier from one flight over the site of US-UMd, which contained numerous scattered clouds. Reflected radiation from the neighboring clouds at US-UMd likely causes the increase in the observed radiance/reflectance. An overestimation of surface albedo is also detected at this site (Fig. 4). For clear-sky cases only, the RMSEs drop to 44.1 W/m^2 for DSR and 27.8 W/m^2 for NSR, respectively. In general, uncertainty in the estimation of surface albedo and NSR is reduced in the calculation of NSR, particularly if both surface albedo and NSR are either overestimated or underestimated.

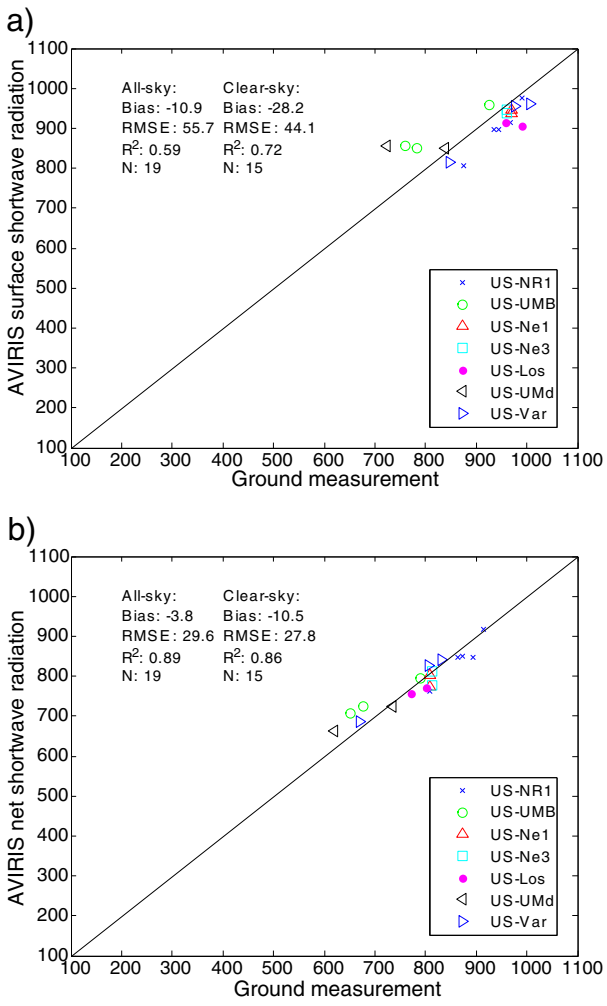

Fig. 7. Validation of (a) DSR and (b) net shortwave radiation (NSR) estimation (W/m^2) at AmeriFlux sites. Statistics are significant at the 95% confidence level.

Results from UCI network sites shown in Fig. 8 indicate that the proposed algorithm works relatively well in mountainous regions but is not as effective as that at AmeriFlux sites, considering that there are

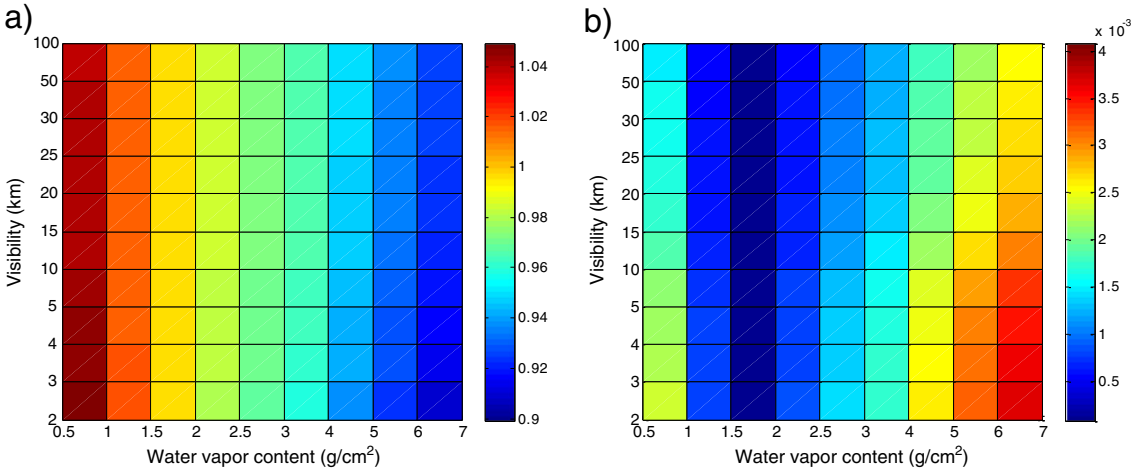

Fig. 6. Water correction factor for estimating downward shortwave radiation (DSR): (a) mean and (b) standard deviation (SDEV). Statistics (W/m^2) were calculated under different atmospheric aerosol loading conditions.

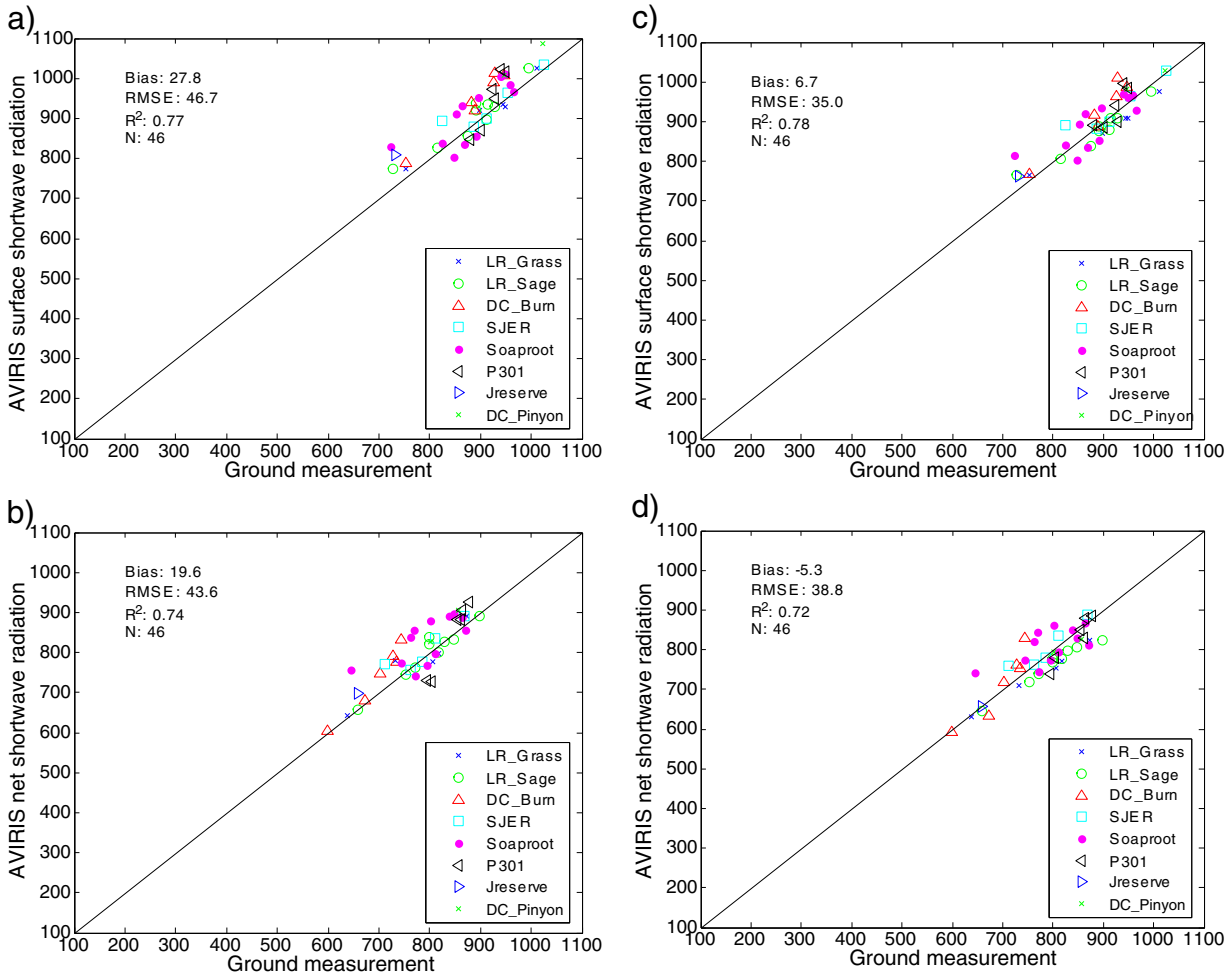

Fig. 8. Validation of DSR and NSR estimation (W/m^2) at UCI sites: (a) DSR and (b) NSR are estimated without topographic correction; (c) DSR and (d) NSR are estimated with topographic correction. Statistics are significant at the 95% confidence level.

only clear-sky cases at the UCI sites. DSR estimation (Fig. 8a) has a bias of 27.8 W/m^2 with an RMSE of 46.7 W/m^2, whereas NSR estimation (Fig. 8b) has a bias of 19.6 W/m^2 with an RMSE of 43.6 W/m^2. A test on the results based on topographic correction shows that the correction resulted in improved accuracy in the estimation, with biases of 6.7 W/m^2 and -5.3 W/m^2 and RMSEs of 35.0 W/m^2 and 38.8 W/m^2 in DSR and NSR estimations, respectively. Unlike the results at the AmeriFlux sites, the NSR estimation is even worse than the DSR estimation at the UCI sites. This occurs likely because an overestimation in surface albedo and an underestimation in DSR would cause a larger underestimation in NSR because of error propagation (e.g., the site of LR_Sage) and vice versa. In addition, because the neighboring effects of diffuse radiation are not considered in the radiation estimation, the uncertainty is generally larger for the UCI sites than for the AmeriFlux sites.

3.3. Direct estimation of NSR (Method B)

Following Eq. (5) and the water vapor correction procedure previously introduced, NSR was directly estimated from the observed radiance. Both stepwise regression and PCA-based regression algorithms were implemented on an angular-bin basis based on simulation data.

Table 2
Statistics of all-sky NSR direct estimation based on simulation data.

	View zenith angle (°)	Solar zenith angle (°)							
		10	15	20	25	30	35	40	45
RMSE (W/m^2)	0	19.32	19.36	19.40	19.42	19.39	19.29	19.09	18.77
	5	19.18	19.35	19.41	19.43	19.43	19.36	19.19	18.91
	10	19.10	19.18	19.37	19.40	19.40	19.35	19.21	18.95
	15	19.15	19.01	19.28	19.32	19.31	19.27	19.15	18.92
	20	19.14	19.01	19.16	19.19	19.18	19.13	19.03	18.82
R^2	0	0.978	0.977	0.975	0.973	0.970	0.967	0.963	0.957
	5	0.978	0.977	0.975	0.973	0.970	0.967	0.962	0.957
	10	0.978	0.977	0.975	0.973	0.970	0.967	0.962	0.956
	15	0.978	0.978	0.976	0.973	0.971	0.967	0.962	0.957
	20	0.978	0.978	0.976	0.974	0.971	0.968	0.963	0.957

Statistics are significant at the 95% confidence level.

PCA-based regression algorithm was found to have better performance over stepwise regression in terms of RMSE and R^2. Statistics for the PCA-based regression algorithm are tabulated in Table 2. Linear regression can achieve an approximate accuracy with ~19 W/m^2 and ~0.97 in RMSE and R^2, respectively, under various surface and atmospheric conditions, which is substantially better than the accuracy achieved when using multispectral data (Kim & Liang, 2010). The results based on simulation data indicate the advantage of hyperspectral data over multispectral data in NSR estimation. Linear regression coefficients have also been calculated exclusively for cloudy-sky simulation data. The corresponding regression accuracy is generally less than 2 W/m^2 in RMSE. In addition, the cloudy-sky coefficients have been applied to the AVIRIS data at the AmeriFlux sites for inter-comparison.

Because Method B did not separate clear-sky and cloudy-sky conditions on a pixel-basis, NSR estimation under both conditions was implemented in the same manner. However, similar to the case of Method A, clouds and shadows lead to difficulty in generating the NSR for the shadow pixels from high-resolution data. Again, for the sake of simplicity, the NSR for the shadow pixels was estimated directly from the NSR of neighboring cloud pixels.

The empirical relationship was then applied to the AVIRIS data for NSR estimation. From the comparison at the AmeriFlux sites (Fig. 9), the difference in water vapor retrievals shows an impact on the NSR estimation, with a difference of ~7 W/m^2 in the estimation bias, particularly for clear-sky conditions. For most sites in Fig. 3, the MODIS product shows a slight underestimation of water vapor compared with AVIRIS retrievals, which is likely the reason for the overestimation of NSR using MODIS data for water vapor correction. Because the AVIRIS water vapor retrieval was made on a pixel basis, it may be more effective at characterizing the spatial variation in water vapor. The AVIRIS-derived water vapor generated slightly different results (<4 W/m^2 difference in RMSE) than those obtained using the MODIS product in the NSR estimation for these sites. However, because there is a lack of simultaneous water vapor in-situ measurements for those AVIRIS flights used in this comparison, it is difficult to make a solid conclusion on which products are better considering the difference in their spatial resolutions and acquisition time.

Applying the cloudy-sky coefficients to the cloudy pixels of all the AVIRIS data over AmeriFlux sites leads to an improved NSR estimation. In this way, the all-sky RMSE in Fig. 9a decreases only by 0.7 W/m^2, which means more efforts are needed for a better consideration for the NSR direct estimation for cloudy-sky cases.

Method B presents an advantage over Method A for cloudy conditions. Because Method B does not separate cloudy and clear-sky conditions in estimating NSR and Method A cannot estimate surface albedo and DSR under cloudy conditions, there are fewer data gaps in the NSR estimation generated from Method B than that from Method A. At the same time, Method B can maintain the NSR estimation accuracy for cloudy cases with RMSE of 36.3 W/m^2 and R^2 of 0.97 ($N = 5$) very similar to that of Method A with RMSE of 35.8 W/m^2 and R^2 of 0.94 ($N = 4$), which however is not statistically significant due to the limited sample size. For high-resolution images, cloud shadows will always result in difficulties in the estimation of surface radiation because of the illumination geometries (i.e., sensor and sun are not on the same side of the cloud), which has been briefly described by Wang et al. (2014). More effort is needed to solve this problem in order to generate reliable NSR estimation under cloudy conditions.

The validation results at the UCI sites shown in Fig. 10 indicate that Method B is robust at different sites with different geolocations, climates, and land cover types, which shows a similar accuracy in NSR estimation (bias: −8.3 W/m^2, RMSE: 45.2 W/m^2). One of the major differences between the two proposed methods is that Method B tends to underestimate NSR compared with Method A. In addition, unlike Method A, the simplified topographic correction method did not generate the results with equivalent accuracy as expected, with a bias of 28.6 W/m^2 and an RMSE of 55.3 W/m^2. This result suggests that a more sophisticated algorithm for topographic correction is needed to generate robust NSR estimation for Method B, which may include an improved consideration on the variation of direct and diffuse DSR components under different topographic conditions (e.g., Long, Gao, & Singh, 2010) and/or a radiative transfer model that handles inhomogeneous

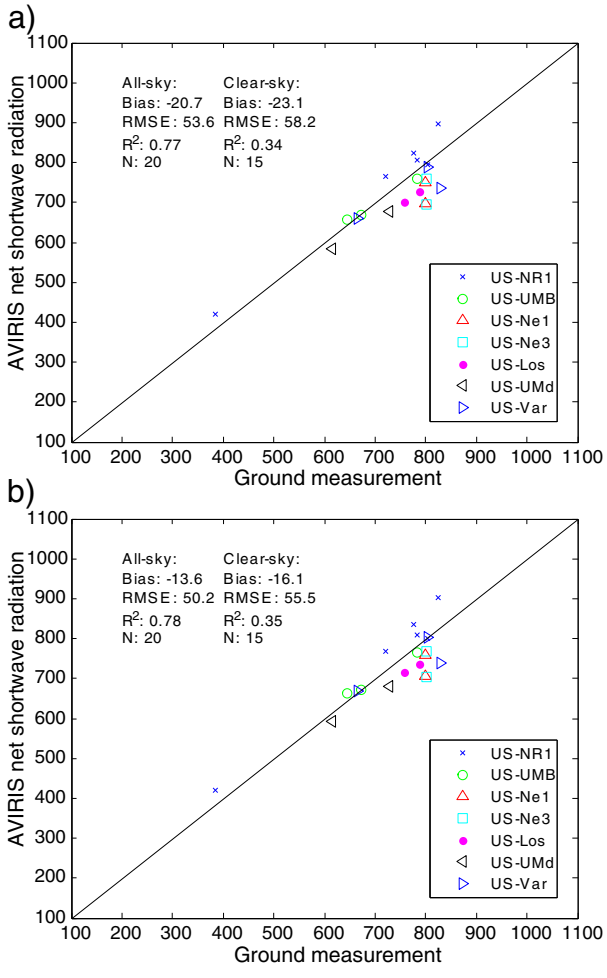

Fig. 9. Validation of NSR direct estimation (W/m^2) at AmeriFlux sites using different water vapor correction inputs: (a) AVIRIS water vapor retrievals; and (b) MODIS water vapor product. Statistics are significant at the 95% confidence level.

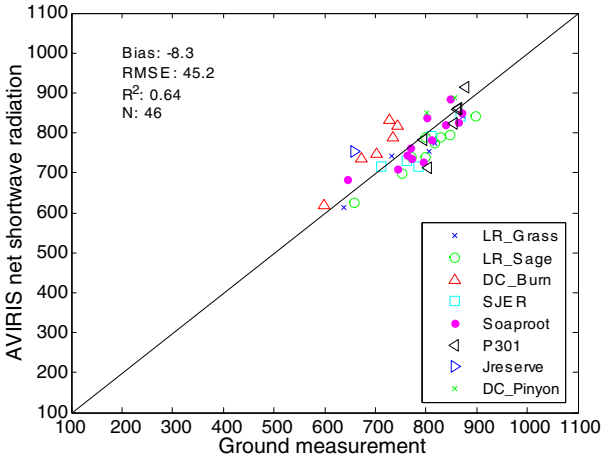

Fig. 10. Validation of NSR direct estimation (W/m^2) at UCI sites. Statistics are significant at the 95% confidence level.

surface albedo and topography (e.g., Mayer, Hoch, & Whiteman, 2010). In addition, because the pyranometers have a much smaller "footprint" in sampling the upward radiation than the downward radiation, they introduce another source of uncertainty in the direct comparison of the pixel-based estimation and ground measurements of NSR if the variations of surface albedo and atmosphere are not adequately accounted for.

4. Conclusions

In this study, hyperspectral remote sensing data were proved to improve accuracies in quantifying the DSR and NSR based on the simulation data. Two methods proposed for instantaneous NSR estimation were validated and inter-compared using the AVIRIS data as proxy to prototype the HyspIRI algorithms at the AmeriFlux and UCI sites, which were found to be able to generate accurate instantaneous NSR estimation with RMSEs of approximately 28–56 W/m^2. Some errors from ground measurements can contribute to the uncertainties found in the validation. Nevertheless, the proposed methods provided much improved results on NSR estimation compared with those in previous studies (Kim & Liang, 2010; Tang, Li, & Zhang, 2006; Wang et al., 2014). It is worthy to note that both methods proposed in this study are very time efficient because the look-up tables and regression coefficients are pre-calculated, which enables their application to future hyperspectral satellite data.

Some major findings of this study are summarized as follows:

1) Water vapor effects were considered in the estimation of DSR and NSR. A difference of ~3–4 W/m^2 (RMSE) in the radiation estimation accuracy was detected when water vapor estimation derived from AVIRIS data was used as the inputs rather than the MODIS product with a coarser resolution. Nevertheless, the level of water vapor content was not sufficiently high to reflect significant improvements in the AVIRIS NSR estimation.
2) A simplified topographic correction method was used to adjust the observed radiance before the estimation of surface radiation budget components, which did not result in significantly improved NSR estimation. Adjacency effects need to be considered in the future refinement of the proposed algorithms for high-resolution remote sensing data, particularly over mountainous regions.
3) The direct estimation method (Method B) has an advantage over the traditional method (Method A) because the former does not separate clear-sky and cloudy-sky conditions in the NSR estimation. Method B provides a possible solution for NSR estimation under cloudy conditions through the constraint of error propagation. However, the limited number of validation data has precluded a solid conclusion on the accuracy assessment particularly for the cloudy cases.

With the availability of more hyperspectral data from the ongoing HyspIRI flight campaign and future HyspIRI satellite mission, extensive investigation on the performance of the proposed method under cloudy conditions will be conducted. Nevertheless, consideration of the horizontal heterogeneity of atmospheric scattering (e.g., aerosols and clouds) must be included in the refinement of the NSR estimation algorithms, particularly for cloudy conditions.

Acknowledgments

This work was funded by the NASA HyspIRI preparatory Grant NNH11ZDA001N-HyspIRI through the University of Maryland, College Park. We thank the AVIRIS team for pre-processing the AVIRIS data. Many thanks to the AmeriFlux network and their PIs for providing ground flux measurements. The radiation observations at the UCI sites in Southern California and Sierra Nevada were supported by the US Department of Energy Terrestrial Ecosystem Science Program (DE-FG02-05ER64021) and the US National Science Foundation Southern Sierra Critical Zone Observatory (1331939), respectively. Special thanks to Dr. Aeron Fellows for his help provide some information of the UCI sites. We also thank the three anonymous reviewers for their very constructive comments.

References

Baldridge, A.M., Hook, S.J., Grove, C.I., & Rivera, G. (2009). The ASTER spectral library version 2.0. *Remote Sensing of Environment*, *113*, 711–715.
Berk, A., Anderson, G.P., Acharya, P.K., Bernstein, L.S., Muratov, L., Lee, J., et al. (2006). MODTRAN5: 2006 update. *Proc. SPIE 6233, Algorithms and Technologies for Multispectral, Hyperspectral, and Ultraspectral Imagery XII*, *62331F*, (pp. 62331 F-62331 F-62338).
Bevis, M., Businger, S., Chiswell, S., Herring, T.A., Anthes, R.A., Rocken, C., et al. (1994). GPS meteorology — Mapping zenith wet delays onto precipitable water. *Journal of Applied Meteorology*, *33*, 379–386.
Bisht, G., & Bras, R.L. (2010). Estimation of net radiation from the MODIS data under all sky conditions: Southern Great Plains case study. *Remote Sensing of Environment*, *114*, 1522–1534.
Bisht, G., & Bras, R.L. (2011). Estimation of net radiation from the Moderate Resolution Imaging Spectroradiometer over the continental United States. *IEEE Transactions on Geoscience and Remote Sensing*, *49*, 2448–2462.
Bisht, G., Venturini, V., Islam, S., & Jiang, L. (2005). Estimation of the net radiation using MODIS (Moderate Resolution Imaging Spectroradiometer) data for clear sky days. *Remote Sensing of Environment*, *97*, 52–67.
Braun, J., & Van Hove, T. (2005). Recent improvements in the retrieval of precipitable water vapor. *ION GNSS 2006*. Long Beach, CA: Institute of Navigation.
Bruegge, C.J., Conel, J.E., Green, R.O., Margolis, J.S., Holm, R.G., & Toon, G. (1992). Water-vapor column abundance retrievals during Fife. *Journal of Geophysical Research-Atmospheres*, *97*, 18759–18768.
Clark, R.N., Swayze, G.A., Wise, R., Livo, E., Hoefen, T., Kokaly, R., et al. (2007). *USGS digital spectral library splib06a. U.S. Geological Survey, Digital Data Series 231*.
Dubayah, R. (1992). Estimating net solar-radiation using Landsat Thematic Mapper and digital elevation data. *Water Resources Research*, *28*, 2469–2484.
Gao, B.C., Goetz, A.F.H., & Wiscombe, W.J. (1993). Cirrus cloud detection from airborne imaging spectrometer data using the 1.38 mu-m water-vapor band. *Geophysical Research Letters*, *20*, 301–304.
Gao, B.C., & Kaufman, Y.J. (2003). Water vapor retrievals using moderate resolution imaging spectroradiometer (MODIS) near-infrared channels. *Journal of Geophysical Research-Atmospheres*, *108*.
Gao, B.C., Montes, M.J., Davis, C.O., & Goetz, A.F.H. (2009). Atmospheric correction algorithms for hyperspectral remote sensing data of land and ocean. *Remote Sensing of Environment*, *113*, S17–S24.
Garcia, M., & Ustin, S.L. (2001). Detection of interannual vegetation responses to climatic variability using AVIRIS data in a coastal savanna in California. *IEEE Transactions on Geoscience and Remote Sensing*, *39*, 1480–1490.
Goulden, M.L., Anderson, R.G., Bales, R.C., Kelly, A.E., Meadows, M., & Winston, G.C. (2012). Evapotranspiration along an elevation gradient in California's Sierra Nevada. *Journal of Geophysical Research — Biogeosciences*, *117*.
Gui, S., Liang, S.L., Wang, K.C., Li, L., & Zhang, X.T. (2010). Assessment of three satellite-estimated land surface downwelling shortwave irradiance data sets. *IEEE Geoscience and Remote Sensing Letters*, *7*, 776–780.
He, T., Liang, S.L., & Song, D.X. (2014a). Analysis of global land surface albedo climatology and spatial–temporal variation during 1981–2010 from multiple satellite products. *Journal of Geophysical Research-Atmospheres*, *119*, 10,281–210,298.
He, T., Liang, S.L., Wang, D., Shi, Q., & Tao, X. (2014b). Estimation of high-resolution land surface shortwave albedo from AVIRIS data. *IEEE Journal of Selected Topics in Applied Earth Observations and Remote Sensing*, *7*.
He, T., Liang, S.L., Wang, D., Shuai, Y., & Yu, Y. (2014c). Fusion of satellite land surface albedo products across scales using a multiresolution tree method in the north central United States. *IEEE Transactions on Geoscience and Remote Sensing*, *52*, 3428–3439.
He, T., Liang, S.L., Wang, D., Wu, H., Yu, Y., & Wang, J. (2012). Estimation of surface albedo and directional reflectance from Moderate Resolution Imaging Spectroradiometer (MODIS) observations. *Remote Sensing of Environment*, *119*, 286–300.
Huang, G.H., Liu, S.M., & Liang, S.L. (2012). Estimation of net surface shortwave radiation from MODIS data. *International Journal of Remote Sensing*, *33*, 804–825.
Hwang, K., Choi, M., Lee, S.O., & Seo, J.W. (2013). Estimation of instantaneous and daily net radiation from MODIS data under clear sky conditions: A case study in East Asia. *Irrigation Science*, *31*, 1173–1184.
Kaufman, Y.J., & Gao, B.C. (1992). Remote sensing of water vapor in the near IR from EOS/MODIS. *IEEE Transactions on Geoscience and Remote Sensing*, *30*, 871–884.
Kiehl, J.T., & Trenberth, K.E. (1997). Earth's annual global mean energy budget. *Bulletin of the American Meteorological Society*, *78*, 197–208.
Kim, H.Y., & Liang, S.L. (2010). Development of a hybrid method for estimating land surface shortwave net radiation from MODIS data. *Remote Sensing of Environment*, *114*, 2393–2402.
Kuusinen, N., Tomppo, E., Shuai, Y., & Berninger, F. (2014). Effects of forest age on albedo in boreal forests estimated from MODIS and Landsat albedo retrievals. *Remote Sensing of Environment*, *145*, 145–153.
Levy, R.C., Remer, L.A., Kleidman, R.G., Mattoo, S., Ichoku, C., Kahn, R., et al. (2010). Global evaluation of the Collection 5 MODIS dark-target aerosol products over land. *Atmospheric Chemistry and Physics*, *10*, 10399–10420.
Li, F.Q., Jupp, D.L.B., Thankappan, M., Lymburner, L., Mueller, N., Lewis, A., et al. (2012). A physics-based atmospheric and BRDF correction for Landsat data over mountainous terrain. *Remote Sensing of Environment*, *124*, 756–770.
Liang, S.L., & Fang, H.L. (2004). An improved atmospheric correction algorithm for hyperspectral remotely sensed imagery. *IEEE Geoscience and Remote Sensing Letters*, *1*, 112–117.

Liang, S.L., Stroeve, J., & Box, J.E. (2005). Mapping daily snow/ice shortwave broadband albedo from Moderate Resolution Imaging Spectroradiometer (MODIS): The improved direct retrieval algorithm and validation with Greenland in situ measurement. *Journal of Geophysical Research-Atmospheres*, *110*.

Liang, S.L., Wang, K.C., Zhang, X.T., & Wild, M. (2010). Review on estimation of land surface radiation and energy budgets from ground measurement, remote sensing and model simulations. *IEEE Journal of Selected Topics in Applied Earth Observations and Remote Sensing*, *3*, 225–240.

Liang, S., Zhang, X., He, T., Cheng, J., & Wang, D. (2013). Remote sensing of the land surface radiation budget. In G.P. Petropoulos (Ed.), *Remote sensing of energy fluxes and soil moisture content* (pp. 125–165). CRC Press.

Liang, S.L., Zheng, T., Liu, R.G., Fang, H.L., Tsay, S.C., & Running, S. (2006). Estimation of incident photosynthetically active radiation from Moderate Resolution Imaging Spectrometer data. *Journal of Geophysical Research-Atmospheres*, *111*.

Liang, S.L., Zheng, T., Wang, D.D., Wang, K.C., Liu, R.G., Tsay, S.C., et al. (2007). Mapping high-resolution incident photosynthetically active radiation over land from polar-orbiting and geostationary satellite data. *Photogrammetric Engineering and Remote Sensing*, *73*, 1085–1089.

Liu, R.G., Liang, S.L., He, H.L., Liu, J.Y., & Zheng, T. (2008). Mapping incident photosynthetically active radiation from MODIS data over China. *Remote Sensing of Environment*, *112*, 998–1009.

Loeb, N.G., Lyman, J.M., Johnson, G.C., Allan, R.P., Doelling, D.R., Wong, T., et al. (2012). Observed changes in top-of-the-atmosphere radiation and upper-ocean heating consistent within uncertainty. *Nature Geoscience*, *5*, 110–113.

Loeb, N.G., Wielicki, B.A., Doelling, D.R., Smith, G.L., Keyes, D.F., Kato, S., et al. (2009). Toward optimal closure of the Earth's top-of-atmosphere radiation budget. *Journal of Climate*, *22*, 748–766.

Long, D., Gao, Y.C., & Singh, V.P. (2010). Estimation of daily average net radiation from MODIS data and DEM over the Baiyangdian watershed in North China for clear sky days. *Journal of Hydrology*, *388*, 217–233.

Mayer, B., Hoch, S.W., & Whiteman, C.D. (2010). Validating the MYSTIC three-dimensional radiative transfer model with observations from the complex topography of Arizona's Meteor Crater. *Atmospheric Chemistry and Physics*, *10*, 8685–8696.

Papaioannou, G., Papanikolaou, N., & Retalis, D. (1993). Relationships of photosynthetically active radiation and shortwave irradiance. *Theoretical and Applied Climatology*, *48*, 23–27.

Pinker, R.T., Frouin, R., & Li, Z. (1995). A review of satellite methods to derive surface shortwave irradiance. *Remote Sensing of Environment*, *51*, 108–124.

Pinker, R.T., & Laszlo, I. (1992). Modeling surface solar irradiance for satellite applications on a global scale. *Journal of Applied Meteorology*, *31*, 194–211.

Qin, J., Yang, K., Liang, S.L., Zhang, H., Ma, Y.M., Guo, X.F., et al. (2011). Evaluation of surface albedo from GEWEX-SRB and ISCCP-FD data against validated MODIS product over the Tibetan Plateau. *Journal of Geophysical Research-Atmospheres*, *116*.

Revercomb, H.E., Turner, D.D., Tobin, D.C., Knuteson, R.O., Feltz, W.F., Barnard, J., et al. (2003). The ARM program's water vapor intensive observation periods — Overview, initial accomplishments, and future challenges. *Bulletin of the American Meteorological Society*, *84*, 217–236.

Roberts, D.A., Quattrochi, D.A., Hulley, G.C., Hook, S.J., & Green, R.O. (2012). Synergies between VSWIR and TIR data for the urban environment: An evaluation of the potential for the Hyperspectral Infrared Imager (HyspIRI) Decadal Survey mission. *Remote Sensing of Environment*, *117*, 83–101.

Roman, M.O., Gatebe, C.K., Schaaf, C.B., Poudyal, R., Wang, Z.S., & King, M.D. (2011). Variability in surface BRDF at different spatial scales (30 m–500 m) over a mixed agricultural landscape as retrieved from airborne and satellite spectral measurements. *Remote Sensing of Environment*, *115*, 2184–2203.

Roman, M.O., Gatebe, C.K., Shuai, Y., Wang, Z., Gao, F., Masek, J.G., et al. (2013). Use of in situ and airborne multiangle data to assess MODIS- and Landsat-based estimates of directional reflectance and albedo. *IEEE Transactions on Geoscience and Remote Sensing*, *51*, 1393–1404.

Roman, M.O., Schaaf, C.B., Woodcock, C.E., Strahler, A.H., Yang, X.Y., Braswell, R.H., et al. (2009). The MODIS (Collection V005) BRDF/albedo product: Assessment of spatial representativeness over forested landscapes. *Remote Sensing of Environment*, *113*, 2476–2498.

Schaepman, M.E., Ustin, S.L., Plaza, A.J., Painter, T.H., Verrelst, J., & Liang, S.L. (2009). Earth system science related imaging spectroscopy—An assessment. *Remote Sensing of Environment*, *113*, S123–S137.

Seyednasrollah, B., & Kumar, M. (2013). Effects of tree morphometry on net snow cover radiation on forest floor for varying vegetation densities. *Journal of Geophysical Research-Atmospheres*, *118*, 12508–12521.

Shi, Q.Q., & Liang, S.L. (2013). Characterizing the surface radiation budget over the Tibetan Plateau with ground-measured, reanalysis, and remote sensing data sets: 1. Methodology. *Journal of Geophysical Research-Atmospheres*, *118*, 9642–9657.

Shuai, Y.M., Masek, J.G., Gao, F., & Schaaf, C.B. (2011). An algorithm for the retrieval of 30-m snow-free albedo from Landsat surface reflectance and MODIS BRDF. *Remote Sensing of Environment*, *115*, 2204–2216.

Stackhouse, J.W.P., Gupta, S.K., Cox, S.J., Mikovitz, J.C., Zhang, T., & Hinkelman, L.M. (2011). The NASA/GEWEX surface radiation budget release 3.0: 24.5-year dataset. *GEWEX News*, *21*, 10–12.

Stephens, G.L., Li, J.L., Wild, M., Clayson, C.A., Loeb, N., Kato, S., et al. (2012). An update on Earth's energy balance in light of the latest global observations. *Nature Geoscience*, *5*, 691–696.

Tang, B.H., Li, Z.L., & Zhang, R.H. (2006). A direct method for estimating net surface shortwave radiation from MODIS data. *Remote Sensing of Environment*, *103*, 115–126.

Tasumi, M., Allen, R.G., & Trezza, R. (2008). At-surface reflectance and albedo from satellite for operational calculation of land surface energy balance. *Journal of Hydrologic Engineering*, *13*, 51–63.

Trenberth, K.E., Fasullo, J.T., & Kiehl, J. (2009). Earth's global energy budget. *Bulletin of the American Meteorological Society*, *90*, 311–323.

Wang, D., Liang, S.L., & He, T. (2014). Mapping high-resolution surface shortwave net radiation from Landsat data. *IEEE Geoscience and Remote Sensing Letters*, *11*, 459–463.

Wang, D., Liang, S.L., He, T., & Yu, Y. (2013). Direct estimation of land surface albedo from VIIRS data: Algorithm improvement and preliminary validation. *Journal of Geophysical Research-Atmospheres*, *118*, 12,577–512,586.

Wang, J., White, K., & Robinson, G.J. (2000). Estimating surface net solar radiation by use of Landsat-5 TM and digital elevation models. *International Journal of Remote Sensing*, *21*, 31–43.

Wen, J.G., Zhao, X.J., Liu, Q., Tang, Y., & Dou, B.C. (2014). An improved land-surface albedo algorithm with DEM in rugged terrain. *IEEE Geoscience and Remote Sensing Letters*, *11*, 883–887.

Wild, M. (2005). Solar radiation budgets in atmospheric model intercomparisons from a surface perspective. *Geophysical Research Letters*, *32*.

Wild, M. (2008). Short-wave and long-wave surface radiation budgets in GCMs: A review based on the IPCC-AR4/CMIP3 models. *Tellus Series A-Dynamic Meteorology and Oceanography*, *60*, 932–945.

Wild, M., Folini, D., Schar, C., Loeb, N., Dutton, E.G., & Konig-Langlo, G. (2013). The global energy balance from a surface perspective. *Climate Dynamics*, *40*, 3107–3134.

Zhang, Y.C., Rossow, W.B., Lacis, A.A., Oinas, V., & Mishchenko, M.I. (2004). Calculation of radiative fluxes from the surface to top of atmosphere based on ISCCP and other global data sets: Refinements of the radiative transfer model and the input data. *Journal of Geophysical Research-Atmospheres*, *109*.

Zheng, T., Liang, S.L., & Wang, K.C. (2008). Estimation of incident photosynthetically active radiation from GOES visible imagery. *Journal of Applied Meteorology and Climatology*, *47*, 853–868.